

**Laser-speckle-visibility acoustic spectroscopy in soft turbid media**Frédéric Wintzenrieth,<sup>1</sup> Sylvie Cohen-Addad,<sup>1,2</sup> Marie Le Merrer,<sup>1</sup> and Reinhard Höhler<sup>1,2</sup><sup>1</sup>Université Paris 6, UMR 7588 CNRS-UPMC, INSP, 4 Place Jussieu, 75252 Paris Cedex 05, France<sup>2</sup>Université Paris-Est, LPM DI, 5 Boulevard Descartes, 77454 Marne-la-Vallée, France

(Received 30 August 2013; revised manuscript received 4 December 2013; published 23 January 2014)

We image the evolution in space and time of an acoustic wave propagating along the surface of turbid soft matter by shining coherent light on the sample. The wave locally modulates the speckle interference pattern of the backscattered light, which is recorded using a camera. We show both experimentally and theoretically how the temporal and spatial correlations in this pattern can be analyzed to obtain the acoustic wavelength and attenuation length. The technique is validated using shear waves propagating in aqueous foam. It may be applied to other kinds of acoustic waves in different forms of turbid soft matter such as biological tissues, pastes, or concentrated emulsions.

DOI: [10.1103/PhysRevE.89.012308](https://doi.org/10.1103/PhysRevE.89.012308)

PACS number(s): 46.35.+z, 43.58.+z, 42.30.-d, 82.70.Rr

**I. INTRODUCTION**

The viscoelastic shear response of soft matter such as foams, concentrated emulsions, self-assembling surfactant systems, pastes, or biological tissues often presents a wide spectrum of mechanical relaxations. The relaxations are due to couplings between processes on molecular and mesoscopic length scales that raise many open questions [1–5]. Capturing these relaxations requires measurements over many decades in frequency, but this requirement is hard to meet experimentally: Inertia limits the scope of conventional rheometers to a range typically below 100 Hz. Rheometers based on torsional resonators do provide complex shear modulus data up to the order of  $10^5$  Hz, but only at a single frequency for a given device geometry [6,7]. Microrheology experiments consist in tracking the Brownian motion of tracer particles dispersed in the sample using either multiple light scattering or direct observation [4,8]. While this method has been successfully applied to actin gels [9] and wormlike micelle suspensions [3], the interpretation of such data requires that the sample can be considered as a viscoelastic continuum at the scale of the probe particles. This criterion is hard to meet in materials such as foams where the typical size of the mesoscopic structure is much larger than that of tracer particles that perform significant Brownian motion. A restriction related to the intrinsic heterogeneity of the sample also limits the scope of the piezorheometers described in the literature [10,11]. They are able to probe the complex shear modulus at frequencies up to the kilohertz range, but their typical gap widths are no larger than typically 100  $\mu\text{m}$ . Besides these rheometry techniques, measuring the speed and attenuation of transverse or longitudinal sound waves is an alternative approach for probing the viscoelastic response of soft matter over an extended range of frequencies [12–14]. However, for complex fluids such as foams where the acoustic impedance mismatch between typical transducers and the sample is very large, this technique is hard to implement and the strong attenuation of transverse sound in foams, pastes, or emulsions raises additional problems.

In this paper we present an experimental method for measuring the dispersion relation and attenuation of shear waves propagating in foams and other turbid complex fluids. It is based on the interaction of a sound wave and diffuse coherent light, used as a probe. When coherent light is backscattered

from a turbid material it gives rise to a speckle interference pattern that is modified as the scatterers contained in the sample move relative to each other [15]. Such diffusing-wave spectroscopy (DWS) measurements have been used to detect sound waves at a given position in suspensions [16]. In samples where the scatterer dynamics are not ergodic, such as biological tissues, the simultaneous detection of many speckles using a camera reveals transient displacements induced by ultrasonic waves in turbid media [17]. The intensity fluctuations are analyzed either by correlation functions or by measuring the normalized variance of the speckle pattern, called visibility, as a function of exposure time of the camera. If the change of the pattern is significant during this time, speckles are averaged out and their visibility decreases. The relation between visibility and sample dynamics is the basis of speckle-visibility spectroscopy (SVS) [18], an experimental technique that has been used to study coarsening dynamics in foams [19] and the flow of granular materials [20]. We go beyond this pioneering work by showing how acoustic wave propagation can be imaged in time as well as in space using speckle correlations. This variant of SVS, which we call laser-speckle-visibility acoustic spectroscopy (LSVAS), is validated in a frequency range accessible with a high-frequency sliding plate rheometer [21,22]. We demonstrate its scope by presenting the measurement of the dispersion relation and the attenuation length of shear waves in an aqueous foam up to 1 kHz.

The speed and attenuation of a shear wave propagating in a viscoelastic material depend on its elastic and viscous properties. The linear viscoelastic response is described by the complex shear modulus  $G^*(\omega) = G'(\omega) + iG''(\omega)$ , where the real part  $G'$  and the imaginary part  $G''$  correspond to the storage and loss moduli, respectively. Their dependences on the angular frequency  $\omega$  are characteristic of the relaxation time spectrum that spans several decades in complex fluids such as foams [21–23], concentrated emulsions [24,25], soft pastes [26], or microgel suspensions [5]. Here we consider aqueous foams whose shear modulus  $G^*$  has been studied in the range of 0.1 mHz to 100 Hz in previous experiments [21–23]. Two generic models predict a power law  $G^* \sim (i\omega)^{1/2}$  at high frequencies [24,27]. However, the experiments evidence deviations from these predictions, calling for further investigations [22].

The paper is organized as follows. Section II briefly recalls how coherent light propagates in turbid materials, as well as the basic principles of diffusing-wave spectroscopy and speckle-visibility spectroscopy. In Sec. III our experimental setup and procedure are presented. In Sec. IV we explain in detail how shear sound velocity and attenuation length are extracted from the speckle-visibility data. In Sec. V dispersion relation and attenuation length data obtained with an aqueous foam are presented and compared to previous results reported in the literature in a restricted range of frequencies. A summary is given in Sec. VI.

## II. THEORETICAL BACKGROUND

To make the paper self-contained, we summarize the bases of diffusing-wave spectroscopy [28] and speckle-visibility spectroscopy [18]. A laser beam injects coherent light into the sample, which may be modeled schematically as a concentrated dispersion of isotropic point scatterers in a transparent matrix. In such a material, light is strongly scattered and propagates along random-walk-like paths. The average distance between successive isotropic scattering events is called the transport mean free path  $\ell^*$ . Propagation along many different paths contributes to the backscattered light observed near a given point outside the sample, leading to a speckle interference pattern. A detector ideally measures the intensity  $I(t)$  of a single speckle in this pattern;  $I(t)$  fluctuates, depending on displacements of the scatterers that modify the phases of the different waves reaching the detector. The purpose of DWS and SVS measurements is to deduce the scatterer dynamics from these speckle intensity fluctuations [15,18,29]. The fluctuations that occur during a delay time  $\tau$  are characterized by the intensity autocorrelation function  $g_2(t, \tau)$ :

$$g_2(t, \tau) \equiv \frac{1}{\beta} \left( \frac{\langle I(t)I(t+\tau) \rangle}{\langle I \rangle^2} - 1 \right). \quad (1)$$

The angular brackets represent an average over all possible realizations of the light random walks. The average can be implemented as a time average if these realizations are successively created by intrinsic stationary internal dynamics of the sample, such as in Brownian suspensions or coarsening foams. To probe transient or nonergodic dynamics, the averaging is performed over an ensemble of speckles, detected using a camera [30,31]. In the following we will focus on this latter variant of DWS, called multispeckle diffusing-wave spectroscopy, where  $g_2$  is a function of time  $t$  as well as delay time  $\tau$ . The normalization parameter  $\beta$  is defined such that  $g_2(t, 0) = 1$ . Its value depends on the detection optics:  $\beta = 1$  for polarized detection and for a detector area so small that the intensity of a single speckle is measured. When the detector area increases, the speckle fluctuations diminish due to the spatial averaging and  $\beta$  decreases [18,32].

Information about the scatterer dynamics can also be extracted from a multispeckle experiment by measuring the visibility of the speckle pattern  $V(T, t)$  as a function of exposure time  $T$ . With increasing  $T$ , the visibility decreases due to the temporal averaging of fluctuations. It is defined as

the normalized variance of the speckle intensity  $I_T$ :

$$V(T, t) \equiv \frac{1}{\beta} \left( \frac{\langle I_T^2 \rangle}{\langle I_T \rangle^2} - 1 \right). \quad (2)$$

The angular brackets denote the average over the ensemble of speckles. In the limit  $T \rightarrow 0$ ,  $V(T, t)$  tends to 1, whereas for  $T \rightarrow \infty$  it decreases asymptotically towards zero.

To interpret visibility or autocorrelation data in terms of scatterer dynamics the electric field correlation function  $g_1(t, \tau)$  is considered. Here  $E(t)$  represents the electric field resulting from the superposition of fields due to all photon paths between the light source and the detector:

$$g_1(t, \tau) \equiv \frac{\langle E(t+\tau)E^*(t) \rangle}{\langle |E(t)|^2 \rangle}. \quad (3)$$

Further,  $g_1(t, \tau)$  and  $g_2(t, \tau)$  are related by the Siegert relation [28]

$$g_2(t, \tau) = |g_1(t, \tau)|^2. \quad (4)$$

The fundamental relation of speckle visibility spectroscopy relates  $V(T)$  and  $g_1(t, \tau)$  [18]:

$$V(T, t) = \int_0^T 2(1 - \tau/T) |g_1(t, \tau)|^2 d\tau / T. \quad (5)$$

The expression of  $g_1(t, \tau)$  given by Eq. (3) is written as a sum of the contributions of each individual path, labeled by an index  $p$ . Phase variations due to scatterer motions accumulate along the paths and induce light interferences at the detector. For each path of curvilinear length  $s$ , we number the successively visited scattering sites by an index  $j$ , going from 1 to  $s/\ell^*$ . The contribution of a path to  $g_1(t, \tau)$  is expressed as a function of  $\Delta\phi_j^p(t, \tau)$ , defined as the variation of the phase difference between the scattering sites  $j$  and  $j+1$  that occurs between the instants  $t$  and  $t+\tau$ , for scattering path number  $p$ . The field correlation function is written as

$$g_1(t, \tau) = \sum_p \frac{\langle I_p \rangle}{\langle I \rangle} \left\langle \exp \left( -i \sum_j \Delta\phi_j^p(t, \tau) \right) \right\rangle. \quad (6)$$

The quantities  $\sum_j \Delta\phi_j^p(t, \tau)$  are considered as Gaussian random variables and thus  $g_1$  can be expressed in terms of their second moments, averaged over the paths that we denote by  $\langle \Delta\phi(t, \tau)^2 \rangle$ . Moreover, the path contributions are weighted by their length distribution  $P(s)$ . Finally, the following expression of the field correlation function is obtained:

$$g_1(t, \tau) = \int_{s=0}^{\infty} P(s) e^{-\langle \Delta\phi(t, \tau)^2 \rangle s / 2\ell^*} ds. \quad (7)$$

Here  $P(s)$  depends on the scattering geometry and is determined by solving the diffusion equation for photons, with appropriate boundary conditions. In the backscattering geometry, the following expression holds, to a good approximation, for a semi-infinite sample [28,33]:

$$g_1(t, \tau) = e^{-\gamma \sqrt{3\langle \Delta\phi(t, \tau)^2 \rangle / 2}}, \quad (8)$$

where  $\gamma$  is a constant typically in the range 1–3, depending on the polarization of the detected backscattered light with respect to that of the incident light and on the anisotropy of the scatterers. Expressions for  $\langle \Delta\phi(t, \tau)^2 \rangle$  in the case of

ballistic or diffusive random motion of the scatterers are provided in the literature [28]. The cases of longitudinal acoustic waves [16] and simple shear strain [34] have also been studied. In Sec. IV A we present an expression of  $\langle \Delta\phi(t, \tau)^2 \rangle$ ,  $g_1(t, \tau)$ , and  $V(T, t)$  for arbitrary time-dependent strain.

We then focus on the shear strain induced by a transverse plane wave propagating in the bulk of a material. Let us call  $\lambda$  and  $\kappa = 2\pi/\lambda$  its wavelength and wave number, respectively, and  $l_A$  the attenuation length that governs the exponential decrease of the strain amplitude with propagation distance. The complex wave number  $\kappa^* = \kappa - i/l_A$  is related to the complex shear modulus by [12]

$$G^*(\omega) = \rho \left( \frac{\omega}{\kappa^*} \right)^2, \quad (9)$$

where  $\rho$  is the density of the material. It can be split into its real and imaginary parts

$$G'(\omega) = \frac{\rho\omega^2[\kappa^2 - 1/l_A^2]}{[\kappa^2 + 1/l_A^2]^2} \quad (10)$$

and

$$G''(\omega) = \frac{2\rho\omega^2\kappa}{l_A[\kappa^2 + 1/l_A^2]^2}. \quad (11)$$

Conversely, if the complex modulus of a viscoelastic fluid is known, the wave number and the attenuation length can be predicted using Eq. (9) as we see in Sec. V.

### III. EXPERIMENT

#### A. Experimental setup

The foam sample is placed in a rectangular trough (of length 12.0 cm, width 8.5 cm, and height 5.0 cm). A rigid plexiglass plate (7.5 cm wide) is aligned perpendicular to the  $x_1$  direction and inserted into the middle of the sample as shown in Fig. 1. The plate is subjected to a sinusoidal translation displacement in the  $x_2$  direction with controlled amplitude  $A_0$  and frequency  $f = \omega/2\pi$ . Here  $A_0$  is chosen in the range 1–10  $\mu\text{m}$ , while  $f$  is varied between 75 and 1300 Hz. Straight grooves are cut into the plate to prevent wall slip. They are 300  $\mu\text{m}$  deep and oriented parallel to the  $x_3$  direction. The plate motion generates an acoustic shear wave in the foam that propagates along the  $x_1$  direction. As we will show in Sec. V, the shear wave is attenuated in the foam over propagation distances smaller than 2 cm. Since this attenuation length is smaller than the distance between the region of the sample probed by the laser beam (see Fig. 1) and the nearest wall of the trough, the influence of the walls on the investigated wave propagation is negligible. In addition, the boundary between the foam and the air above has no significant impact on the shear wave propagation, as demonstrated in the Appendix. Our experiment therefore yields the propagation characteristics of bulk shear waves.

A linearly polarized laser beam (633-nm wavelength) shines on the top surface of the sample. It is expanded by diffraction through a circular pinhole so that a spot of lateral extent close to 4 cm is obtained. The backscattered intensity is collected by a eight-bit complementary metal-oxide semiconductor (CMOS) camera (AVT Marlin F131B,

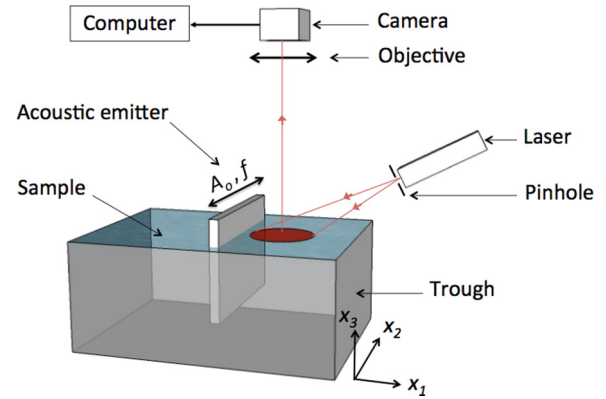


FIG. 1. (Color online) Experimental setup. An expanded laser beam shines on the top surface of a turbid foam sample in the region highlighted in red. The volume where the foam is probed by the light extends a few scattering mean free paths into the sample volume. The backscattered light forms a speckle interference pattern that is recorded using a camera. It is equipped with an objective, allowing speckle fluctuations to be detected as a function of the position at the sample surface. The acoustic emitter consists of a plate inserted into the sample and translated sinusoidally along the  $x_2$  direction, with frequency  $f$  and displacement amplitude  $A_0$ . This plate generates an acoustic shear bulk wave that propagates through the scattering volume in the  $x_1$  direction.

square pixels of size  $6.7 \mu\text{m} \times 6.7 \mu\text{m}$ ) via an objective (Nikkon AF Micro Nikkor). Its diaphragm aperture is set so that the size of the coherence area at the camera detector is of the order of the size of one pixel, yielding for the parameter  $\beta$  typically a value of 0.2. Each speckle that reaches the camera corresponds to a specific region of the sample surface, allowing the acoustic wave propagation to be resolved in space. The objective is slightly out of focus so that the structure of individual bubbles is not resolved and the recorded spatial intensity variations are due only to speckle interference. The acquisition rate  $R$ , exposure time  $T$ , and number of pixels per image are adjusted for each frequency  $f$  to enable the stroboscopic light detection scheme presented in Sec. IV B. In practice, the smallest exposure time  $T$  used is 0.39 ms with an acquisition rate of 325 frames/s ( $300 \times 200$  pixels per image), while the longest one is 27 ms with 19 frames/s and  $1200 \times 200$  pixels per image.

The foam gas volume fraction  $\varphi$  is deduced from the electrical conductivity of the foam using the relationship given in [35]. To obtain the conductivity we measure the electrical impedance at a frequency of 3 kHz, between two electrodes (not shown in Fig. 1) that are flush mounted in one of the vertical walls of the trough, 5 mm below the top surface of the sample.

#### B. Experimental protocol

We study foam samples composed of Gillette shaving foam (Normal Regular), which is known to be very stable: Bubbles do not coalesce, the drainage of the liquid content is slow, and the structure evolves mainly due to coarsening, induced by diffusive gas exchange between bubbles [23]. Initially foam is injected into the trough until it slightly overflows

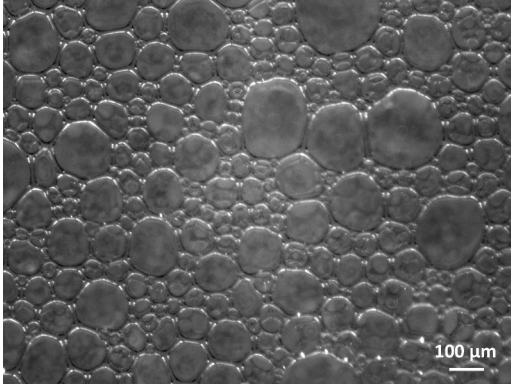


FIG. 2. Typical foam structure viewed at the surface of the sample. The average bubble diameter is  $d = 75 \mu\text{m}$  and the gas volume fraction is  $\varphi = 94.2\%$ .

it and the sample surface is smoothed out. As the foam age (defined as the time elapsed since production) increases, the top layer of the sample that is in contact with the ambient air expands. This artifact is not due to coarsening, but to an osmotic effect: The gas contained in Gillette foam is an alcane mixture and therefore air diffuses into the bubbles. Prior to each acoustic measurement the inflated top layer of the sample is removed and photographs of the surface are taken using a video microscope (see Fig. 2). Using these images, we measure the size of about 200 bubbles and deduce the average bubble diameter  $d$  as well as the normalized standard deviation, denoted by  $\mu_2$ .

For a given sample, the acoustic frequency  $f$  is kept fixed and the wavelength and attenuation length are measured at a time interval of 20 min for foam ages between 25 and 125 min. The parameters  $\lambda$  and  $l_A$  corresponding to a given bubble size (i.e., foam age) are interpolated from the measurements of  $\lambda$  and  $l_A$  as a function of time. The evolution of the gas volume fraction  $\varphi$  is monitored by conductivity measurements. As the foam ages, it undergoes a slow drainage due to gravity so that  $\varphi$  slightly increases with time. At the end of the experiment, the trough is filled with a new sample and the protocol is repeated with another frequency. The investigated frequencies span 75–1300 Hz. We thus determine the acoustic foam properties at four average bubble sizes: (a)  $d = 45 \pm 5 \mu\text{m}$ ,  $\varphi = (93.2 \pm 0.3)\%$ ; (b)  $d = 62 \pm 5 \mu\text{m}$ ,  $\varphi = (93.5 \pm 0.4)\%$ ; (c)  $d = 75 \pm 5 \mu\text{m}$ ,  $\varphi = (93.8 \pm 0.5)\%$ ; and (d)  $d = 95 \pm 5 \mu\text{m}$ ,  $\varphi = (94.2 \pm 0.5)\%$ . The standard deviation of bubble diameter distribution, normalized by the average diameter, is in all cases  $\mu_2 = 0.58 \pm 0.04$ . The light scattering mean free path in foam with such gas volume fractions is equal to 3.5 times the bubble diameter [36]. All measurements are performed at a temperature of 22 °C.

#### IV. LASER-SPECKLE-VISIBILITY ACOUSTIC SPECTROSCOPY

##### A. Diffuse light propagation in the presence of an acoustic wave

We use the formalism of DWS and SVS recalled in Sec. II to calculate how the speckle pattern backscattered from the surface of a turbid material is modulated in the presence of an acoustic wave. As a first step, we consider how the

distance  $D$  between two scattering sites  $j$  and  $j + 1$  that are successively encountered by a propagating light wave depends on the local strain, described by the infinitesimal strain tensor  $\varepsilon$ . The region probed by a backscattered photon has a typical radius of a few scattering mean free paths  $\ell^*$  [19]. Therefore, the strain is homogeneous in this region if  $|\kappa^* \ell^*| \ll 1$ . In this case, elementary continuum kinematics yield the following linearized expression of  $D$  with the usual summation convention for indices [37]:

$$D = \ell^* [1 + \varepsilon_{mn} u_m u_n], \quad (12)$$

where  $u_m$  is a unit vector pointing from site  $j$  to site  $j + 1$ . As time evolves from  $t$  to  $t + \tau$ , the strain changes by an amount denoted by  $\Delta \varepsilon_{mn}(t, \tau)$  and this leads to a variation of  $D$  that we write as  $\Delta D(t, \tau)$ :

$$\Delta D(t, \tau) = \ell^* \Delta \varepsilon_{mn}(t, \tau) u_m u_n. \quad (13)$$

The variation of the light phase that accompanies the change of  $D$  is  $\Delta \phi(t, \tau) = k \Delta D(t, \tau)$ , where  $k$  is the light wave number. To predict the field correlation function defined in (3) we must calculate the average of  $\Delta \phi(t, \tau)^2$  along a light path. Since the light propagates along random-walk trajectories, the step leading from  $j$  to  $j + 1$  can have any orientation in space. We therefore average  $\Delta \phi(t, \tau)^2$  over all possible directions of the unit vector  $\mathbf{u}$  and write the result in terms of invariants of the symmetric strain tensor so that it is valid in any frame of reference:

$$\langle \Delta \phi(t, \tau)^2 \rangle = (k \ell^*)^2 \{ [\text{Tr}(\Delta \varepsilon)]^2 + 2 \text{Tr}(\Delta \varepsilon^2) \} / 15. \quad (14)$$

The invariant  $\text{Tr}(\Delta \varepsilon)$  expresses relative changes of volume. The remaining invariant  $\text{Tr}(\Delta \varepsilon^2)$  can be considered as an isotropic measure of deviatoric (shear) deformation. Many equivalent expressions and specific cases of Eq. (14) have been discussed in the literature [16,34,38–40], going back to pioneering work by Wu *et al.* [38] and Bicout *et al.* [39]. Substituting Eq. (14) into Eq. (8) yields the strain dependence of  $g_1$  in the case of a backscattering experiment:

$$g_1(t, \tau) = \exp \left( -\gamma k \ell^* \sqrt{[\text{Tr}(\Delta \varepsilon)]^2 + 2 \text{Tr}(\Delta \varepsilon^2)} / 10 \right). \quad (15)$$

The elastic response of disordered materials such as foams is homogeneous only on a macroscopic length scale, much larger than a bubble diameter. At a scale of the order of the bubble size, much smaller than  $\lambda$  in our experiments, the response is heterogeneous and the strain tensor components  $\varepsilon_{mn}$  fluctuate around their macroscopic average values  $\langle \varepsilon_{mn} \rangle$ , where the angular brackets represent an average over the fluctuations encountered along a photon path. Strictly speaking, the expressions  $\text{Tr}(\Delta \varepsilon^2)$  and  $[\text{Tr}(\Delta \varepsilon)]^2$  in Eq. (14) should therefore be replaced by  $\langle \text{Tr}(\Delta \varepsilon^2) \rangle$  and  $[\langle \text{Tr}(\Delta \varepsilon) \rangle]^2$ . We consider only a linear mechanical response where  $\varepsilon_{mn} \propto \langle \varepsilon_{mn} \rangle$ . In view of Eq. (14) this means that a locally heterogeneous mechanical response modifies the value of  $\langle \Delta \phi(t, \tau)^2 \rangle$  calculated for a homogeneous response by a constant coefficient. Equation (15) shows that in this case  $g_1$  behaves as if the strain amplitude  $\varepsilon_0$  had an effective value that is enhanced by a constant factor. We will not investigate this effect further here since such a modification of  $\varepsilon_0$  has no impact on the measurements of the

acoustic wavelengths and attenuation lengths described in the following.

We now focus on the case of isochoric strain [ $\text{Tr}(\Delta\varepsilon) = 0$ ] induced by an acoustic shear wave of wave number  $\kappa^*$  and angular frequency  $\omega$ . It travels in the  $x_1$  direction through a material whose elastic response is assumed to be homogeneous. As a starting point, we consider the displacement  $\vec{U}(x_1, t)$ , where  $\vec{e}_2$  is the unit vector in the transverse direction  $x_2$ :

$$\vec{U}(x_1, t) = A_0 e^{-x_1/l_A} \sin(\kappa x_1 - \omega t) \vec{e}_2. \quad (16)$$

Here  $A_0$  is the displacement amplitude at the emitter where  $x_1 = 0$ . The only nonzero components of the strain tensor deduced from this displacement field are

$$\begin{aligned} \varepsilon_{12} &= \varepsilon_{21} \\ &= \frac{A_0}{2} e^{-x_1/l_A} \left[ -\frac{1}{l_A} \sin(\kappa x_1 - \omega t) + \kappa \cos(\kappa x_1 - \omega t) \right]. \end{aligned} \quad (17)$$

The two trigonometric functions can be combined as

$$\begin{aligned} \varepsilon_{12} &= \frac{\kappa A_0}{2} e^{-x_1/l_A} \sqrt{1 + (\kappa l_A)^{-2}} \\ &\times \cos[\kappa x_1 - \omega t + \arctan(\kappa^{-1} l_A^{-1})]. \end{aligned} \quad (18)$$

We thus see that the acoustic attenuation has two effects on the strain oscillation: At a given frequency, it introduces a constant phase shift  $\arctan(\kappa^{-1} l_A^{-1})$  and it has an influence on the amplitude of the strain oscillation, which may be written as  $\varepsilon_0 = \exp(-x_1/l_A) \frac{A_0}{2} \kappa \sqrt{1 + (\kappa l_A)^{-2}}$ . To simplify, we choose the origin of time such that the phase is set to zero and finally write

$$\varepsilon_{12}(x_1, t) = \varepsilon_0 \cos(\kappa x_1 - \omega t). \quad (19)$$

Using Eqs. (15) and (19), we predict the dependence of  $g_1$  on position  $x_1$ , time  $t$ , and delay time  $\tau$ :

$$\begin{aligned} g_1(x_1, t, \tau) &= \exp\{-\sqrt{2/5} \varepsilon_0 \gamma k \ell^* |\cos[\kappa x_1 - \omega(t + \tau)] \\ &\quad - \cos(\kappa x_1 - \omega t)|\}. \end{aligned} \quad (20)$$

Inserting this result into Eq. (5) yields the modulation of backscattered speckle visibility as a function of exposure time  $T$ , strain amplitude  $\varepsilon_0$ , position  $x_1$ , and time  $t$ :

$$\begin{aligned} V(T, t, x_1) &= \int_0^T 2(1 - \tau/T) \exp[-2\sqrt{2/5} \varepsilon_0 \gamma k \ell^* \\ &\quad \times |\cos(\kappa x_1 - \omega t - \omega\tau) - \cos(\kappa x_1 - \omega t)|] d\tau/T. \end{aligned} \quad (21)$$

In the limit of small exposure times  $T \rightarrow 0$ , the strain variation that the material undergoes during  $T$  remains negligible. In this case, the photon paths are not modified during a snapshot. The visibility remains equal to 1 throughout the sample and provides no information about the acoustic wave propagation. For small but finite exposure times, up to the order of  $2\pi/\omega$ , the visibility is modulated in space and time and in Sec. IV B we show how the shear wave phase velocity can be deduced from these variations. In the limit of large  $\omega T$ , the temporal average of visibility measured as a function of position reveals

the decay of the acoustic wave amplitude with propagation distance. This feature will be discussed in Sec. IV C.

## B. Wavelength and phase velocity measurement

In this section we consider wave propagation over distances  $x_1 \ll l_A$  so that the strain amplitude  $\varepsilon_0$  is constant. Analyzing Eq. (21) generally requires a numerical integration, but the case of small amplitudes  $k\ell^*\varepsilon_0 \ll 1$  and exposure times  $\omega T \ll 1$  can be studied analytically. An expansion to first order in  $\omega T$  and  $\varepsilon_0$  yields

$$V(T, t, x_1) = 1 - \frac{4\omega T \varepsilon_0 \gamma k \ell^*}{3\sqrt{10}} |\sin(\kappa x_1 - \omega t)|. \quad (22)$$

Figure 3 illustrates the predictions of Eqs. (21) and (22). The visibility varies as a function of the phase  $\kappa x_1 - \omega t$  of the acoustic wave. This modulation increases with strain amplitude [Fig. 3(a)] or exposure time [Fig. 3(b)]. For  $\omega T \ll 1$  and  $\varepsilon_0 = 10^{-3}$ , the visibility is maximum whenever the strain goes through an extremum and its evolution is accurately predicted by the linearized mode leading to Eq. (22). With increasing  $\varepsilon_0$  or  $\omega T$  nonlinear corrections set in. In addition,

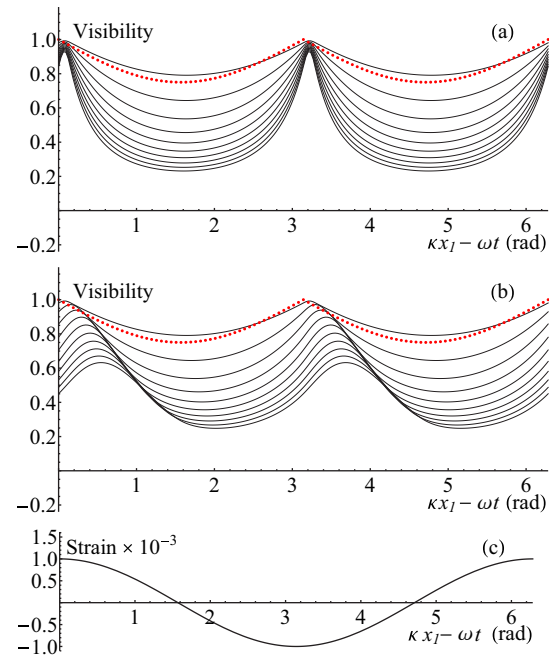


FIG. 3. (Color online) Speckle visibility  $V(T, t, x_1)$  and shear strain  $\varepsilon_{12}$  versus the phase of the acoustic wave  $\kappa x_1 - \omega t$ . (a) The continuous curves are predicted by Eq. (21) for different strain amplitudes  $\varepsilon_0 = n \times 10^{-3}$ , where  $n$  takes integer values ranging from 1 (top curve) to 10 (bottom curve) and an exposure time such that  $\omega T = \pi/10$ . The visibility decreases monotonically as a function of  $n$ . (b) The continuous curves are predicted by Eq. (21) for a strain amplitude  $\varepsilon_0 = 10^{-3}$  and different exposure times such that  $\omega T = n\pi/10$ , where  $n$  takes integer values ranging from 1 (top curve) to 10 (bottom curve). The visibility decreases monotonically with  $n$ . In both (a) and (b) the red dotted line indicates the prediction of the linearized expression (22) for  $\varepsilon_0 = 10^{-3}$  and  $\omega T = \pi/10$ . In all cases, we assume  $\gamma = 1.5$ ,  $\beta = 1$ ,  $\ell^* = 100 \mu\text{m}$ , and a light wavelength of 500 nm. (c) The oscillating shear strain is illustrated for an amplitude  $\varepsilon_0 = 10^{-3}$ .

with increasing  $\omega T$  the phase of the visibility oscillations is more and more shifted with respect to that of the strain oscillations [Fig. 3(b)]. However, the period of the visibility oscillations is always half that of the acoustic wavelength.

In a space-time diagram where gray levels represent visibility as a function of propagating distance  $x_1$  and time  $t$ , a pattern of alternating parallel bright and dark stripes is expected. Each stripe of a given gray level [or visibility (22)] is associated with a constant phase  $\kappa x_1 - \omega t$ . The slope  $dx_1/dt$  yields the phase velocity of the shear strain wave. Thus a space-time diagram provides an image of the propagating wave, in terms of amplitude and phase, that can be used to determine the dispersion relation.

To measure such data experimentally, we record snapshots of the backscattered speckle pattern versus  $x_1$ , at times  $t$  such that the phase  $\omega t$  of the oscillating plate at  $x_1 = 0$  has controlled values covering the range between 0 and  $2\pi$ . A set of snapshots acquired at a rate well above the acoustic frequency can be used to record efficiently the phase evolution during several periods of the wave propagation. However, this does not mean that a high-speed camera is required to perform a speckle visibility acoustic experiment. A stroboscopic image capture using an exposure time  $T$  smaller than  $1/\omega$  yields equivalent data at an acquisition rate  $R$  lower than the acoustic frequency. The phase of the acoustic wave upon the  $n$ th snapshot is  $\kappa x_1 - n\omega/R$ . We choose

$$R = \frac{\omega}{2\pi(N + \delta N)}, \quad (23)$$

where  $N$  is an integer sufficiently large so that  $R$  remains slightly below the maximum acquisition rate of the camera;  $N$  is the number of entire temporal periods of the acoustic wave between two successive snapshots. Changing  $N$  has no impact on the strain observed on the snapshots since the acoustic phase is in this case modified by an integer multiple of  $2\pi$ . The parameter  $\delta N$  is chosen such that  $0 < |\delta N| \ll 1$  and it adjusts the strain phase shift  $-2\pi(N + \delta N)$  between two successive snapshots. Thus, in a stroboscopic sequence of snapshots the visibility oscillates by a factor  $|1 + N/\delta N|$  more slowly than in a continuous observation as a function of time  $t$ . As a consequence, the frequency limits of a speckle-visibility acoustic experiment are set by the accuracy of timing and shutter control rather than by the maximum acquisition rate of the camera.

To obtain visibility data that are statistically robust, a large number of independent speckles must be recorded for each propagation time  $t$  and distance  $x_1$ . Therefore, the extent in the  $x_2$  direction of the region captured by the snapshots is chosen such that for any given propagation distance, at least 100 independent speckles are obtained.

Figure 4 shows a typical experimental space-time plot acquired at a frequency close to 100 Hz. The time axis has been rescaled by the factor  $|1 + N/\delta N|$  so that the quantity  $\omega t$  expresses the phase shift of the acoustic wave as if no stroboscopic detection had been used. The diagram presents indeed the expected pattern of alternating parallel bright and dark stripes discussed above. Their slope  $dx_1/dt$  is equal to the phase velocity of the visibility (22), which has spatial and temporal periods that are both twice those of the acoustic wave. Thus the slope is also equal to the acoustic phase velocity. To

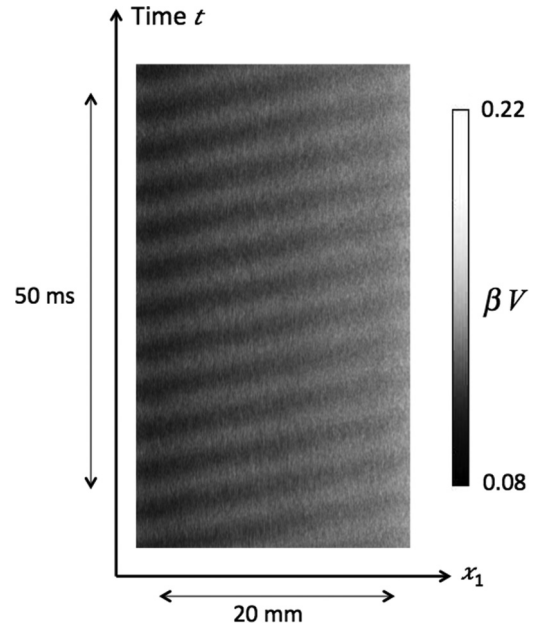


FIG. 4. Space-time plot of the visibility as a function of time  $t$  and propagation distance  $x_1$ , derived from snapshots at successive instants. The gray level is proportional to the level of visibility as indicated by the grayscale chart. The bright stripes correspond to instants and positions where the speckle visibility is maximal [see Eq. (22)], i.e., where the acoustic wave signal goes through an extremum (see Fig. 3). The acoustic wave frequency is 99.5 Hz, the amplitude displacement  $A_0 = 9.2 \mu\text{m}$ , and the exposure time  $T = 5.0 \text{ ms}$ . The stroboscopic acquisition parameters are  $R = 100$  frames per second,  $N = 1$  and,  $1/\delta N = -200$  [see the text for the definition of these notations and Eq. (23)]. The sample is Gillette foam, with average bubble diameter  $d = 48 \mu\text{m}$  and gas volume fraction  $\varphi = (93.7 \pm 0.4)\%$ .

extract quantitatively the acoustic wave velocity, we determine the fundamental Fourier component of the temporal visibility modulation for fixed positions  $x_1$ . Figure 5 shows that the measured phase of this component  $\Phi_V$  increases linearly with propagation distance  $x_1$ . The slope of the fitted straight line is equal to  $2\kappa$ . We then deduce the phase velocity of the acoustic wave as  $c = \omega/\kappa$ .

### C. Attenuation length measurement

We consider that, due to dissipation, the strain amplitude  $\varepsilon_0(x_1)$  of a plane acoustic wave decreases exponentially with propagation distance  $x_1$ . To obtain the length  $l_A$  that characterizes such a decay from the speckle data, the temporal average of the visibility, denoted by  $\bar{V}$ , is calculated. We focus on the case of small acoustic strain amplitudes  $\varepsilon_0 \ll 1$  and linearize the exponential function in Eq. (21):

$$V(T, t, x_1) = 1 - 8\sqrt{\frac{2}{5}} \frac{\varepsilon_0 \gamma k \ell^*}{T} \int_0^T \left(1 - \frac{\tau}{T}\right) \left| \sin\left(\frac{\omega\tau}{2}\right) \right| \times \sin\left(\kappa x_1 - \omega t - \frac{\omega\tau}{2}\right) d\tau. \quad (24)$$

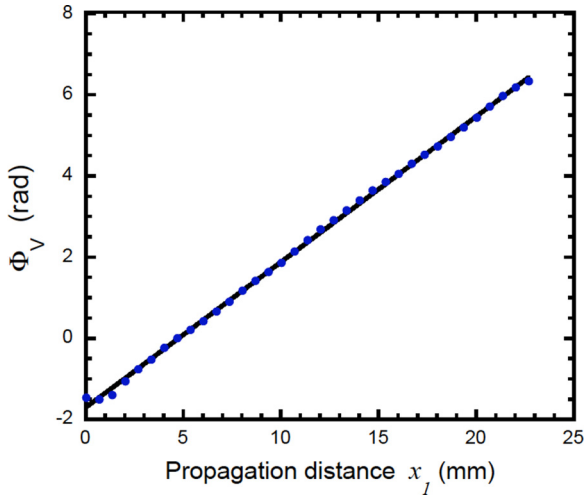


FIG. 5. (Color online) Phase  $\Phi_V$  of the visibility Fourier component at angular frequency  $\omega$  calculated from the space-time plot shown in Fig. 4 as a function of propagation distance. The data are represented by the symbols. The line corresponds to a linear regression to the data: The slope is  $(0.358 \pm 0.002)$  rad  $\text{mm}^{-1}$ . This is equal to twice the acoustic wave number  $\kappa = 0.18$  rad  $\text{mm}^{-1}$ . We deduce the acoustic phase velocity  $c = \omega/\kappa = 3.5$  m  $\text{s}^{-1}$ .

By averaging over the time  $t$ , we obtain  $\bar{V}$ :

$$\bar{V}(\varepsilon_0(x_1), \omega T) = 1 - \frac{16}{\pi} \sqrt{\frac{2}{5}} \gamma k \ell^* S(\omega T) \varepsilon_0(x_1), \quad (25)$$

with

$$S(\omega T) = \frac{1}{T} \int_0^T \left(1 - \frac{\tau}{T}\right) |\sin(\omega\tau/2)| d\tau. \quad (26)$$

Using these results, the strain amplitude can be deduced from the time-averaged visibility. The impacts on  $\bar{V}$  of the acoustic angular frequency  $\omega$  and the exposure time  $T$  are captured by the factor  $S(\omega T)$ , which increases linearly with  $\omega T$  for  $\omega T \ll 1$  and converges to the asymptomatic value 0.32 for  $\omega T$  larger than  $\approx 6$ , as illustrated in Fig. 6. In this limit of exposure times much longer than the acoustic wave period, the sensitivity of the visibility is optimized and independent of the exposure time  $T$ ; we denote it by  $\bar{V}(\varepsilon_0)$ . As long as  $\omega T$

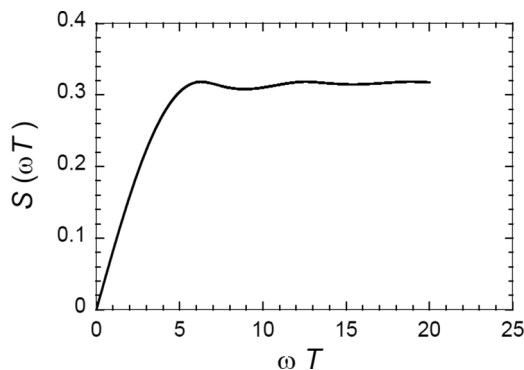


FIG. 6. Variation of the function  $S$  defined in Eq. (26) with the parameter  $\omega T$ .

is kept constant,  $1 - \bar{V}$  is linearly related to  $\varepsilon_0$ :

$$\varepsilon_0(x_1) \sim \frac{1 - \bar{V}(\varepsilon_0)}{\gamma k \ell^*}. \quad (27)$$

We use this result to study the decay of the acoustic wave amplitude with propagation distance. The speckle fluctuations are measured in the vicinity of the acoustic emitter and the variation of the average visibility  $\bar{V}$  with  $x_1$  is extracted. To determine the normalization constant  $\beta$  [Eq. (2)] we record an image in the absence of acoustic waves and calculate the first and second moments of its intensity distribution. Since at rest the average visibility is equal to 1 (neglecting noise and intrinsic sample dynamics), these data yield  $\beta$ . If  $\varepsilon_0(x_1)$  decays exponentially with  $x_1$ , Eq. (27) predicts that  $\ln[1 - \bar{V}(\varepsilon_0(x_1))]$  decreases linearly with  $x_1/l_A$ , so  $l_A$  can easily be extracted from experimental data. Figure 7(a) illustrates that we observe indeed such behavior for small strain amplitudes. However, we note that Eq. (25) is obtained by describing the sample as a dispersion of isotropic point scatterers in a viscoelastic matrix. This simple model may not be justified in all forms of turbid soft matter. In addition, we recall that the approximations leading to Eq. (27) hold only for small strain amplitudes.

To overcome these restrictions, we use a different experimental procedure that only requires that the visibility is a monotonically decreasing function of strain amplitude and that the viscoelastic response is linear and homogeneous throughout the sample. The average visibilities are recorded as a function of propagation distance for two acoustic emitter displacement amplitudes  $A_0$  and  $\xi A_0$ . For an exponential decay, the strain amplitudes vary in these two cases as  $A(x_1) = A_0 e^{-x_1/l_A}$  and  $A(x_1) = A_0 \xi e^{-x_1/l_A} = A_0 e^{-x_1/l_A + \ln \xi}$ . Changing the emitter amplitude by a factor  $\xi$  has the same effect as a translation of the curve  $1 - \bar{V}(\varepsilon_0(x_1))$  by a distance  $l_A \ln(\xi)$  along the  $x_1$  axis. We therefore expect that for a given sample and frequency, plots of visibility versus  $x_1$  obtained for different amplitude ratios  $\xi$  can be superposed on a master curve by applying offsets  $l_A \ln(\xi)$  to the propagation distance. The existence of such a master plot validates the hypothesis of linear mechanical response that our analysis relies on.

To implement and test this method experimentally, we apply to a foam sample successively four displacement amplitudes  $A_0$  in the range between 3.2 and 9.2  $\mu\text{m}$ , with a frequency of 100 Hz. Figure 7(a) shows that, as expected, the visibility  $\bar{V}$  grows with increasing propagation distance  $x_1$  and that at a given distance  $\bar{V}$  decreases with increasing emitter amplitude. By shifting the curves in Fig. 7(a) along the  $x_1$  axis so that the least-squares differences between the curves are minimized, we obtain the well defined master curve shown in Fig. 7(b). The values of  $\xi$  and the shift displacements consistently yield the attenuation length  $l_A = 11.9 \pm 0.1$  mm. Figure 7(a) also shows an exponential fit to the data obtained at the two lowest emitter amplitudes. As pointed out above, the inverses of the slopes on these semilogarithmic plots are expected to yield  $-l_A$ . The results, 12 mm for  $A_0 = 3.2 \mu\text{m}$  and 10.8 mm for  $A_0 = 4.5 \mu\text{m}$ , are consistent with the value of  $l_A$  deduced from the master plot; the small discrepancy may be due to noise. This result validates our model leading to Eq. (27). Figure 7(a) also shows that with increasing excitation amplitudes the relation between  $1 - \bar{V}(\varepsilon_0(x_1))$  and  $x_1$  progressively becomes

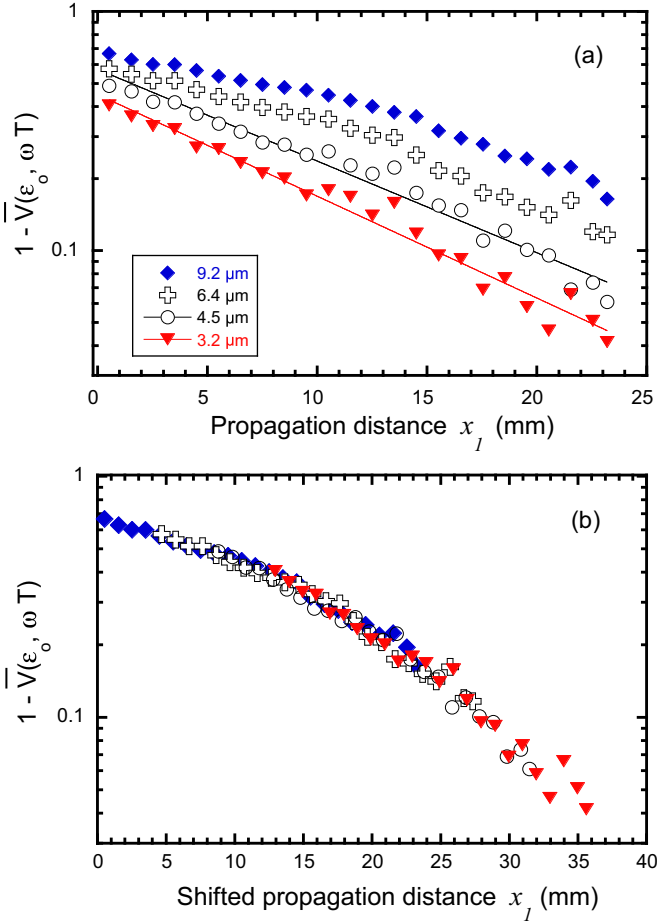


FIG. 7. (Color online) (a) Visibility  $\bar{V}(\epsilon_0, \omega T)$ , defined in Eq. (25), with  $\omega T = 4\pi$ , versus propagation distance  $x_l$ , measured with a foam sample ( $d = 51 \mu\text{m}$ ,  $\phi = 93.8\%$ ) at a frequency  $f = 100 \text{ Hz}$  and exposure time  $T = 20 \text{ ms}$ . The symbols correspond to different displacement amplitudes as labeled in the graph. The speckle data are binned using 28 pixels per bin. The error bars are smaller or of the size of the symbols. The two straight lines are exponential fits, yielding attenuation lengths  $l_A = 10.8 \text{ mm}$  for  $A_0 = 4.5 \mu\text{m}$  and  $l_A = 12 \text{ mm}$  for  $A_0 = 3.2 \mu\text{m}$ . (b) The same data collapsed on a master curve after an offset  $l_A \ln(\xi)$  is applied to the distance  $x_l$ , with  $l_A = 11.9 \text{ mm}$ . The reference curve corresponds to the amplitude  $A_0 = 9.2 \mu\text{m}$ . The symbols are the same as in (a).

nonlinear. In this regime the linearized model (27) no longer applies. Mechanical nonlinearities are very unlikely to be relevant in the present context since the highest investigated strain amplitude is well below 0.1%, which is more than two orders of magnitude below the yield strain of Gillette foam reported in the literature [41].

## V. EXPERIMENTAL RESULTS WITH AQUEOUS FOAMS

For the determination of the wavelength, the exposure time  $T$  is adjusted at each frequency such that  $\omega T = \pi$  and the stroboscopic detection scheme is used (see Sec. IV B). For the attenuation length measurements, we use the method described in Sec. IV C. The exposure time  $T$  is adjusted so that  $\omega T = 4\pi$ , which is in the asymptotic regime shown in Fig. 6. Figures 8 and 9 provide an overview of the experimentally

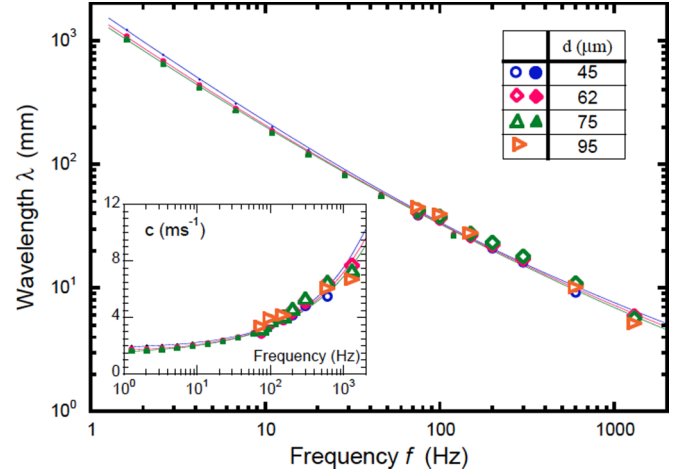


FIG. 8. (Color online) Acoustic wavelength versus frequency measured for aqueous foam (Gillette shaving foam) with different average bubble diameters  $d$  as labeled. The open symbols correspond to the data measured using laser speckle visibility spectroscopy (this study) while the closed symbols are deduced using Eqs. (10) and (11) from previous rheological measurements performed for the same foam and bubble sizes [21]. The solid lines represent the wavelength predicted by the viscoelastic constitutive model (28) with the following parameters:  $d = 45 \mu\text{m}$ ,  $G_0 = 222 \text{ Pa}$ ,  $f_c = 26 \text{ Hz}$ , and  $\eta_0 = 0.26 \text{ Pa s}$  (blue);  $d = 62 \mu\text{m}$ ,  $G_0 = 160 \text{ Pa}$ ,  $f_c = 12 \text{ Hz}$ , and  $\eta_0 = 0.21 \text{ Pa s}$  (red); and  $d = 75 \mu\text{m}$ ,  $G_0 = 136 \text{ Pa}$ ,  $f_c = 8 \text{ Hz}$ , and  $\eta_0 = 0.18 \text{ Pa s}$  (green). The inset shows the phase velocity  $c = \lambda f$  for the same data and model predictions, with the same legend for the symbols.

determined acoustic shear wave propagation characteristics. Using laser-speckle-visibility acoustic spectroscopy (LSVAS),

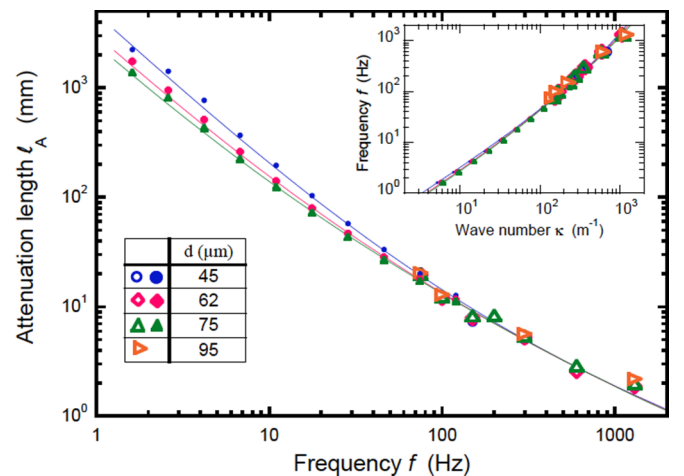


FIG. 9. (Color online) Attenuation length versus frequency measured for the same foam and bubble diameter (as labeled) as in Fig. 8. The open symbols correspond to laser-speckle-visibility spectroscopy data (this study) while the closed symbols are deduced using Eqs. (10) and (11) from previous rheological measurements performed with a rheometer for the same foam and bubble sizes (data from Ref. [21]). The solid lines represent the attenuation length predicted by the viscoelastic model (28) with the same parameters as in Fig. 8. The inset shows the frequency versus wave number for the same samples, with the same legend for the symbols.

we have obtained the wavelength and attenuation length for frequencies between 75 and 1300 Hz and bubble sizes between 45 and 75  $\mu\text{m}$ . In the same figures, we show data at frequencies up to 100 Hz deduced using Eq. (9) from previous complex shear modulus measurements on the same foam for the same bubble diameter and gas volume fraction [21]. These reference data match very well those obtained using LSVAS in the frequency range 75–100 Hz where the two data sets overlap. The attenuation lengths shown in Fig. 9 are all smaller than 2 cm. Therefore, our claim in Sec. III A that the boundary conditions at walls and the bottom of the trough have no impact on the investigated wave propagation is justified.

Experimental complex shear modulus data for Gillette foam at frequencies below 100 Hz are well described by the relation [21], inspired by a model that has previously been proposed to describe the viscoelastic response in concentrated emulsions [24]:

$$G^*(f) = G_0(1 + \sqrt{if/f_c}) + 2\pi i\eta_0 f, \quad (28)$$

where  $G_0$  is the static shear modulus,  $f_c$  is a characteristic relaxation frequency, and  $\eta_0$  reflects the dissipation due to the liquid phase. Substituting Eq. (28) into Eq. (9) yields the following viscoelastic dispersion relation:

$$\kappa^* = \omega \sqrt{\frac{(1 - \varphi)\rho_l}{G_0(1 + \sqrt{i\omega/(2\pi f_c)}) + i\eta_0\omega}}, \quad (29)$$

where  $\rho_l$  is the density of the foaming solution. The wavelength and the attenuation length deduced from Eq. (29) are represented as a function of the frequency by the solid curves in Figs. 8 and 9. The parameters  $G_0$ ,  $f_c$ , and  $\eta_0$  are those previously deduced from measurements below 100 Hz for the same bubble diameters [21]. Our data are thus in good agreement with an extrapolation of current models to frequencies that are an order of magnitude higher than those investigated previously. However, this result obtained for Gillette foam, which has a very high interfacial rigidity, may not be of general validity. Recent experiments with foams based on surfactant solutions with smaller interfacial modulus have evidenced significant deviations from Eq. (28) that increase with frequency [22]. Future LSVAS experiments will allow the investigation of this behavior. We finally note that in the frequency range 100–300 Hz, the transverse sound velocity in Gillette foam with a bubble diameter of 45  $\mu\text{m}$  is smaller than 5  $\text{m s}^{-1}$  (see the inset of Fig. 8). In view of the weak dependence of the velocity on the bubble size evidenced by our data, this result is consistent with the conjecture by Le Goff *et al.* that the surface waves whose observation they report [42] behave as supershear Rayleigh waves that propagate faster than bulk shear waves.

## VI. CONCLUSION

We present laser-speckle-visibility acoustic spectroscopy, a technique for imaging an acoustic shear wave propagating parallel to the surface of a soft turbid material. To detect this wave, we illuminate the sample surface with coherent light and measure how the strain induced by the wave modulates in space and time the backscattered speckle interference pattern. The shutter time of the camera used for these observations

needs to be short compared to the acoustic wave oscillation period, but the time interval between successive snapshots can be much slower if stroboscopic detection is used. Our theoretical analysis and the experimental validation show that from the speckle images, the attenuation length and dispersion relation can be determined without any knowledge of the parameters that characterize the diffusive light propagation in the material. The only requirements are a light scattering mean free path small compared to the acoustic wavelength and, for the attenuation measurement, a linear acoustic response. To minimize the statistical errors of the measurement, a large number of speckles must be acquired for a given propagation time and region of interest. Due to the aging of the samples used in our validation experiments, the disorder of their structure evolves continuously, so averaging over the sample age can be used to average over different realizations of the speckle pattern. In samples that do not have such intrinsic dynamics, enhanced averaging can be obtained by inserting a multiple-scattering disk in the path of the laser light shining on the sample. A slow rotation of this disk will continuously renew the speckle pattern [43]. Moreover, our validation experiments are carried out with acoustic shear waves that are polarized parallel to the sample surface, but LSVAS measurements can be performed just as well with compression waves or surface waves. The detected waves do not need to be plane or coherent; the acoustic propagation can even be diffusive. These features allow mode conversion of waves interacting with an obstacle or the transformation of coherent into diffusive waves to be studied. In a conventional acoustic transmission experiment, the detected intensity depends not only on the sample properties, but also on the acoustic reflections and transmissions on the way from the emitter to the receiver. Therefore, several measurements at different propagation distances are necessary to determine the attenuation length and the propagation speed. In the case of LSVAS, an extended range of propagation distances is probed in a single experiment. This feature distinguishes LSVAS from previous experiments where multiple light scattering was used to detect acoustic vibrations at a single position in a sample. In our validation experiment LSVAS was applied to a homogeneous material, but the technique can also be used to map the acoustic properties of samples that are spatially heterogeneous. Such imaging is called elastography and it is used as a medical diagnostic technique [44]. In this context, LSVAS might, for instance, be useful for detecting skin cancer. Concerning the foam samples used in our validation experiment, we have shown that a previously proposed model of the fast viscoelastic response extends to frequencies an order of magnitude above those that could be investigated previously. Additional experiments in such an extended frequency range with foams of different interfacial rheological behaviors may bring fresh insight into the underlying relaxation mechanism.

To conclude, we have shown that speckle-visibility acoustic spectroscopy is a versatile probe for acoustic wave propagation and viscoelastic response in turbid soft matter such as foams, emulsions, pastes, granular matter, or biological tissues. It extends the scope of previous techniques by direct imaging of propagation or localized acoustic waves in space and time.

## ACKNOWLEDGMENTS

We thank J.-L.Thomas and A. Spadoni for fructuous discussions and C. Blanchard for technical help. We gratefully acknowledge financial support from the European Space Agency (Contract No. MAP AO 99-108) and the Centre National d'Etudes Spatiales (agreement CNES/CNRS No. 127233). M.L.M. was supported by a postdoctoral fellowship from the Centre National d'Etudes Spatiales.

## APPENDIX

In this appendix we discuss the impact of the mechanical boundary conditions on the shear wave propagation experiment illustrated in Fig. 1. For the reasons given in Sec. III A, we do not take into account the vertical walls of the trough containing the foam and model a wave motion that is invariant with respect to translations in the  $x_2$  direction. At  $x_3 = 0$  the sample is in contact with a rigid boundary (the bottom of the trough) where the displacement vector  $\vec{U}$  is zero. The region  $0 < x_3 \leq H$  is filled with foam; at  $x_3 > H$  there is air. The displacement field  $\vec{U}$  in the foam obeys the following equation of motion:

$$\Delta \vec{U} = \frac{\rho}{G^*} \frac{\partial^2 \vec{U}}{\partial t^2}. \quad (\text{A1})$$

The components  $U_1$  and  $U_3$  are zero in the mode of wave propagation excited in our experiment. The solution of Eq. (A1) that satisfies the boundary condition at  $x_3 = 0$  is [45]

$$U_2 = A_0 \sin(\xi x_3) e^{i(\kappa^* x_1 - \omega t)}. \quad (\text{A2})$$

The amplitude  $A_0$  is set by the emitter vibration, whereas the parameter  $\xi$  must obey the following relation, obtained by substituting  $U_2$  given by Eq. (A2) into Eq. (A1):

$$\xi^2 = \frac{\rho \omega^2}{G^*} - \kappa^{*2}. \quad (\text{A3})$$

The displacement in the foam described by Eq. (A2) is accompanied by oscillations of the shear stress components  $\sigma_{12}$  and  $\sigma_{23}$ . Only the latter yields forces at the top surface of the foam:

$$\sigma_{23} = G^* \frac{\partial U_2}{\partial x_3}. \quad (\text{A4})$$

In the plane  $x_3 = H$  we get

$$\sigma_{23} = A_0 G^* \xi \cos(\xi H) e^{i(\kappa^* x_1 - \omega t)}. \quad (\text{A5})$$

If the air did not have any viscosity, the stress  $\sigma_{23}$  in the plane  $x_3 = H$  would have to be zero and the propagation modes would then correspond to  $\xi H = \pi/2 + K\pi$ , where  $K \geq 0$  is an integer. Here  $K$  sets the number of zeros of the function  $U_2(x_3)$  that oscillates for  $x_3$  ranging from 0 to  $H$ . Since the plate that excites the acoustic wave in our experiment imposes a displacement where  $U_2$  is independent of  $x_3$  down to the vicinity of the sample bottom, the propagation mode with  $K = 0$  is expected to be dominant. Moreover, since the density and viscosity of air are very small compared to that of the sample material, we expect the solutions in presence of air to be close to those calculated for a free top boundary. We

therefore write

$$\xi H = \pi/2 + b \quad (\text{A6})$$

and expect the correction  $b$  due to the presence of air to be small compared to  $\pi/2$ . This conjecture will be validated below in the case of our experimental conditions.

We now turn to the displacement and stress fields in the air, which are denoted by  $U'_2$  and  $\sigma'_{23}$ , respectively. Here, there is a diffusive spatial decay of the velocity, governed by the Navier-Stokes equation. We use its linearized form because the velocity amplitude at the foam surface  $A_0\omega$ , set by the motion of the wave emitter, is orders of magnitude smaller than the sound velocity in air. For a shear excitation in the  $x_2$  direction we obtain

$$\Delta \frac{\partial U'_2}{\partial t} = \frac{1}{\nu} \frac{\partial^2 U'_2}{\partial t^2}, \quad (\text{A7})$$

where  $\nu$  is the kinematic viscosity of air. We use the ansatz

$$U'_2 = A'_0 e^{-\delta(x_3-H)} e^{i(\kappa^* x_1 - \omega t)}. \quad (\text{A8})$$

By substituting  $U'_2$  into Eq. (A7) we obtain

$$\delta^2 = \kappa^{*2} - i \frac{\omega}{\nu}. \quad (\text{A9})$$

The viscous stress in the air at  $x_3 = H$  reads

$$\sigma'_{23}(H) = \eta \left. \frac{\partial^2 U'_2}{\partial x_3 \partial t} \right|_{x_3=H} = i A'_0 \delta \eta \omega e^{i(\kappa^* x_1 - \omega t)}, \quad (\text{A10})$$

where  $\eta$  is the dynamic viscosity of air. Continuity of the stresses at  $x_3 = H$  expressed by Eqs. (A5) and (A10) yields

$$A_0 G^* \xi \cos(\xi H) = i A'_0 \delta \eta \omega. \quad (\text{A11})$$

Continuity of the displacements at  $x_3 = H$  expressed by Eqs. (A8) and (A2) yields

$$A_0 \sin(\xi H) = A'_0. \quad (\text{A12})$$

Combining the last two expressions, we get

$$G^* \xi \cot(\xi H) = i \delta \eta \omega. \quad (\text{A13})$$

A series development to first order in  $b$  of this equation yields, using Eq. (A6),

$$\pi b G^* = -2i \delta \eta \omega H. \quad (\text{A14})$$

We combine this result with Eq. (A9) and obtain

$$b = \frac{2\eta \omega H}{\pi G^*} \sqrt{i \frac{\omega}{\nu} - \kappa^{*2}}. \quad (\text{A15})$$

We now perform a first-order development in  $b$  of Eq. (A3), using Eq. (A6):

$$\frac{(\pi/2 + b)^2}{H^2} = \frac{\pi^2/4 + \pi b}{H^2} = \frac{\rho \omega^2}{G^*} - \kappa^{*2}. \quad (\text{A16})$$

Using Eq. (A15) to eliminate  $b$ , we finally obtain

$$\left( \frac{\pi}{2H} \right)^2 + \frac{2\eta\omega}{G^*H} \sqrt{i \frac{\omega}{\nu} - \kappa^{*2}} = \frac{\rho \omega^2}{G^*} - \kappa^{*2}. \quad (\text{A17})$$

This result must be compared to the dispersion relation (9) of shear waves propagating in the bulk of an infinite sample considered in Sec. II. It reduces to the dispersion relation of

shear waves propagating in the bulk of an infinite sample if the left-hand side is neglected. The first term on the left-hand side of Eq. (A17) takes into account that the sample is bounded and the second term captures the viscous coupling with the air. The characteristic length  $(\nu/\omega)^{1/2}$  that appears in this term scales as the thickness of the viscous boundary layer [46]. Using the viscosity and the density of air, as well as the complex shear modulus of foam determined in our experiment and in previous work, we solve Eq. (A17) numerically and find that for frequencies larger than 75 Hz, the real and imaginary parts of the wave vector deviate by less than 1% from the values for shear waves propagating in the bulk of an infinite sample.

Our calculation also yields that the ratio  $\varepsilon_{23}/\varepsilon_{12}$  at the sample surface ( $x_3 = H$ ) may be expressed as

$$\frac{\varepsilon_{23}}{\varepsilon_{12}} = \frac{\sigma_{23}}{\sigma_{12}} = \frac{\eta \omega \delta}{G^* \kappa^*} = \frac{\eta \omega}{\kappa^* G^*} \sqrt{\kappa^{*2} - i \frac{\omega}{\nu}}. \quad (\text{A18})$$

In the parameter range investigated in our experiments the modulus of this ratio is smaller than  $10^{-3}$ , showing that the strain amplitude  $|\varepsilon_{23}|$  is indeed very small compared to the dominant strain  $|\varepsilon_{12}|$ . We finally conclude that the wave propagation characteristics measured in our experiment are very close to those of shear waves traveling in the bulk of foam.

- 
- [1] R. Höhler and S. Cohen-Addad, *J. Phys.: Condens. Matter* **17**, R1041 (2005).
- [2] S. Cohen-Addad, R. Höhler, and O. Pitois, *Annu. Rev. Fluid Mech.* **45**, 241 (2013).
- [3] N. Willenbacher, C. Oelschlaeger, M. Schopferer, P. Fischer, F. Cardinaux, and F. Scheffold, *Phys. Rev. Lett.* **99**, 068302 (2007).
- [4] D. Wirtz, *Annu. Rev. Biophys.* **38**, 301 (2009).
- [5] M. Cloitre, *Yielding, Flow, and Slip in Microgel Suspensions: From Microstructure to Macroscopic Rheology* (Wiley, New York, 2011), pp. 285–311.
- [6] G. Fritz, W. Pechhold, N. Willenbacher, and N. J. Wagner, *J. Rheol.* **47**, 303 (2003).
- [7] N. Willenbacher and C. Oelschlaeger, *Curr. Op. Colloid Interface Sci.* **12**, 43 (2007).
- [8] T. M. Squires and T. G. Mason, *Annu. Rev. Fluid Mech.* **42**, 413 (2010).
- [9] T. H. Larsen and E. M. Furst, *Phys. Rev. Lett.* **100**, 146001 (2008).
- [10] R. Bartolino and G. Durand, *Phys. Rev. Lett.* **39**, 1346 (1977).
- [11] M. Roth, M. D’Acunzi, D. Vollmer, and G. K. Auernhammer, *J. Chem. Phys.* **132**, 124702 (2010).
- [12] J. D. Ferry, *Viscoelastic Properties of Polymers* (Wiley, New York, 1980).
- [13] N. Mujica and S. Fauve, *Phys. Rev. E* **66**, 021404 (2002).
- [14] J. Pierre, F. Elias, and V. Leroy, *Ultrasonics* **53**, 622 (2013).
- [15] D. A. Weitz, J. X. Zhu, D. J. Durian, H. Gang, and D. J. Pine, *Phys. Scr. T* **49B**, 610 (1993).
- [16] W. Leutz and G. Maret, *Physica B* **204**, 14 (1995).
- [17] E. Bossy, A. R. Funke, K. Daoudi, A.-C. Boccara, M. Tanter, and M. Fink, *Appl. Phys. Lett.* **90**, 174111 (2007).
- [18] R. Bandyopadhyay, A. S. Gittings, S. S. Suh, P. K. Dixon, and D. J. Durian, *Rev. Sci. Instrum.* **76**, 093110 (2005).
- [19] A. S. Gittings and D. J. Durian, *Phys. Rev. E* **78**, 066313 (2008).
- [20] P. K. Dixon and D. J. Durian, *Phys. Rev. Lett.* **90**, 184302 (2003).
- [21] K. Krishan, A. Helal, R. Höhler, and S. Cohen-Addad, *Phys. Rev. E* **82**, 011405 (2010).
- [22] S. Costa, R. Höhler, and S. Cohen-Addad, *Soft Matter* **9**, 1100 (2013).
- [23] A. D. Gopal and D. J. Durian, *Phys. Rev. Lett.* **91**, 188303 (2003).
- [24] A. J. Liu, S. Ramaswamy, T. G. Mason, H. Gang, and D. A. Weitz, *Phys. Rev. Lett.* **76**, 3017 (1996).
- [25] P. Hébraud, F. Lequeux, and J.-F. Paliarne, *Langmuir* **16**, 8296 (2000).
- [26] C. Derec, A. Ajdari, G. Ducouret, and F. Lequeux, *Phys. Rev. E* **67**, 061403 (2003).
- [27] B. P. Tighe, E. Woldhuis, J. J. C. Remmers, W. van Saarloos, and M. van Hecke, *Phys. Rev. Lett.* **105**, 088303 (2010).
- [28] D. A. Weitz and D. J. Pine, *Diffusing-Wave Spectroscopy* (Clarendon, Oxford, 1993), Chap. 16, pp. 652–720.
- [29] G. Maret and P. E. Wolf, *Z. Phys. B* **65**, 409 (1987).
- [30] S. Cohen-Addad and R. Höhler, *Phys. Rev. Lett.* **86**, 4700 (2001).
- [31] S. Kirsch, V. Frenz, W. Schartl, E. Bartsch, and H. Sillescu, *J. Chem. Phys.* **104**, 1758 (1996).
- [32] E. Jakeman, C. J. Oliver, and E. R. Pike, *J. Phys. A* **3**, L45 (1970).
- [33] R. Höhler, V. Labiausse, and S. Cohen-Addad, *J. Opt. Soc. Am. A* **20**, 2179 (2003).
- [34] R. Höhler, S. Cohen-Addad, and H. Hoballah, *Phys. Rev. Lett.* **79**, 1154 (1997).
- [35] K. Feitosa, S. Marze, A. Saint-Jalmes, and D. J. Durian, *J. Phys.: Condens. Matter* **17**, 6301 (2005).
- [36] D. J. Durian, D. A. Weitz, and D. J. Pine, *Science* **252**, 686 (1991).
- [37] L. D. Landau and E. M. Lifshitz, *Theory of Elasticity*, 3rd ed., Course of Theoretical Physics Vol. 7 (Elsevier, Amsterdam, 1986).
- [38] X.-L. Wu, D. J. Pine, P. M. Chalkin, J. S. Huang, and D. A. Weitz, *J. Opt. Soc. Am. B* **7**, 15 (1990).
- [39] D. Bicut, E. Akkermans, and R. Maynard, *J. Phys. France I* **1**, 471 (1991).
- [40] M. Erpelding, R. M. Guillemic, B. Dollet, A. Saint-Jalmes, and J. Crassous, *Phys. Rev. E* **82**, 021409 (2010).
- [41] F. Rouyer, S. Cohen-Addad, R. Höhler, P. Sollich, and S. M. Fielding, *Eur. Phys. J. E* **27**, 309 (2008).
- [42] A. Le Goff, P. Cobelli, and G. Lagubeau, *Phys. Rev. Lett.* **110**, 236101 (2013).
- [43] P. Zakharov, F. Cardinaux, and F. Scheffold, *Phys. Rev. E* **73**, 011413 (2006).
- [44] S. Catheline, J.-L. Gennisson, G. Delon, M. Fink, R. Sinkus, S. Abouelkaram, and J. Culioli, *J. Acoust. Soc. Am.* **116**, 3734 (2004).
- [45] K. F. Graff, *Wave Motion in Elastic Solids* (Dover, New York, 1975).
- [46] G. K. Batchelor, *An introduction to Fluid Dynamics* (Cambridge University Press, Cambridge, 2000).